Available online at www.sciencedirect.com
ScienceDirect
Journal of Nuclear Materials 359 (2006) 29–40
journal of nuclear materials
www.elsevier.com/locate/jnucmat

Experimental partial phase diagram of the Zr–Sn–Fe system

N. Nieva [a,*], D. Arias [b]

[a] Departamento de Física, FCEyT, Laboratorio de Física del Sólido, Universidad Nacional de Tucumán. Av. Independencia 1800, 4000 S.M. de Tucumán, Argentina

[b] Departamento de Materiales, CAC, Comisión Nacional de Energía Atómica, Av. Del Libertador 8250, 1429 Buenos Aires, Argentina

Received 6 December 2004; accepted 18 July 2006

Abstract

Results of the experimental study of the phase diagram of the zirconium–tin–iron ternary system are presented. The existing phases and their equilibrium relationships in an extended area of the Gibb's triangle, for 800 and 900 °C isothermal sections, are analyzed. For the experimental work, a set of ternary alloys was designed, produced and examined by different complementary techniques: quantitative analysis with electron-probe microanalysis (EPMA), qualitative analysis with electron scanning microscopy and X-ray energy dispersive spectrometry (EDS), X-ray diffraction and metallographic examination (with optic and electronic microscopy). Phase transformations associated with the Zr-rich region of the system were investigated with electrical resistance vs. temperature measurements. The resultant ternary phase diagram is outlined.

PACS: 81.30.Bx

1. Introduction

The study of phase diagrams and phase transformations is very important in almost all the branches of metallurgy and materials science. The revisions of the phase diagrams based on experimental results, on the analysis of the preceding knowledge of the system of interest, and on the comparison with similar systems allow the continuous update of the knowledge.

The alloys based on zirconium (Zr) are of extended application in the nuclear industry. They are used mainly as cladding and structural material in light and heavy water nuclear reactors. They are used due to three main characteristics: good mechanical properties, low cross section of neutron absorption and good resistance to corrosion.

A type of alloy frequently employed in the nuclear field is Zircaloy, with the chemical composition shown in Table 1. In the process of manufacturing, tin (Sn) is added by means of a master alloy of Zr–Sn–Fe, with a high content of Sn in its composition (usually a composition near to: Zr (20%)–Sn (70%)–Fe (10%) in at.%).

Information on experimental results of the phase diagrams of the mentioned ternary system is scarce. Tanner and Levinson [1] in 1960 studied the Zr–Sn–Fe phase diagram in the region located between the

* Corresponding author. Tel.: +54 381 4252464; fax: +54 381 4363004.
E-mail address: nnieva@herrera.unt.edu.ar (N. Nieva).

0022-3115/$ - see front matter © 2006 Elsevier B.V. All rights reserved.
doi:10.1016/j.jnucmat.2006.07.014

Table 1
Chemical composition of the Zr-based alloys Zircaloy-2 and Zircaloy-4 (at.%) (Zr balance)

	Zircaloy-2	Zircaloy-4
Sn	1.2–1.7%	1.2–1.7%
Fe	0.07–0.2%	0.18–0.24%
Cr	0.05–0.15%	0.07–0.13%
Ni	0.03–0.08%	
O	0.14% max.	0.14% max.

Zr corner, the compound Zr_4Sn and the compound $ZrFe_2$, between 200 °C and 1100 °C. They did not recognize the presence of the Zr_3Fe and Zr_2Fe intermetallics in the ternary diagrams that they reported (they were based on a binary Zr–Fe diagram established in 1951 by Hayes et al. [2] which did not show those two compounds). Tanner and Levinson [1] reported the existence of a ternary phase (they called it θ-phase) with composition: Zr (68.6%)–Sn (19.0%)–Fe (12.4%) in at.%. Afterward, Kudriatsev et al. [3] in 1968 analyzed the Zr-rich region of the Zr–Sn–Fe system from microstructure studies and measurements of hardness and micro-hardness. In their results, Kudriatsev et al. did not register the presence of the ternary θ-phase. Later, Korotkova [4], based on the work of Tanner and Levinson [1], studied the Zr (90%)–Fe $(10-x)$%–Sn (x%) with $0 < x < 10\%$ (at.%) isopleth of the ternary Zr–Sn–Fe diagram. Korotkova proposed a sequence of reactions for the region located between the pure Zr, and the Zr_5Sn_3 and $ZrFe_2$ intermetallics, but Korotkova did not outline any isothermal section. In 1990, Kwon et al. [5] determined the crystalline structure of the θ-phase. In this work, like Tanner and Levinson [1] and Korotkova [4], the authors indicated that this compound has a very narrow single-phase region and denoted it as Zr_6Sn_2Fe. They verified that it is a compound of hexagonal structure, Zr_6Al_2Co type, with lattice parameters $a = 0.7967$ nm and $c = 0.3486$ nm. Finally, a revision of the Zr–Sn–Fe system was published in 1992 by Raghavan [6] and is mainly based on the results of Tanner and Levinson [1], Kudriatsev et al. [3], and Korotkova [4]. Raghavan outlined two 'tentative' isothermal sections (700 °C and 1100 °C) based on the reactions scheme from Korotkova, with no details of the Zr-rich region. There are no updated versions reported of the 800 and 900 °C isothermal sections on this system. On the other hand, Nieva and Arias [7,8] analyzed the region of the phase diagram located near the composition of the mentioned master alloy of Zircaloy, and found two new ternary compounds in this system, sited in the central region of the Zr–Sn–Fe Gibb's triangle. They called them as N-phase and X-phase.

The objective of the present work was the experimental study and revision of the phase diagrams of the Zr–Sn–Fe ternary system for the 800 and 900 °C isothermal sections. The work is divided in two parts. The part 1 is focused in the adjustment of the phase diagrams in the region located between the Zr-rich corner and the pseudo-binary Zr_5Sn_3–$ZrFe_2$. A set of thirteen ternary alloys was prepared for the review of this region. On the other hand, the results of the part 2 partially cover the region located between the above mentioned pseudo-binary and the Sn-rich corner. There are no published results of this ternary region except the previous reported works by the authors [7,8]. A set of seven alloys was analyzed for the part 2.

The existing phases and their equilibrium relationships in these regions of the Gibb's triangle surface, for 800 and 900 °C isothermal sections, were examined. The alloys were thermally treated and analyzed by means of a set of complementary

Table 2
Nominal compositions (at.% and wt%) of the manufactured alloys (Parts 1 and 2)

Alloy denomination	Composition (at.%)			Composition (wt%)		
	Zr	Sn	Fe	Zr	Sn	Fe
Part 1						
m01	76.9	7.4	15.7	80.0	10.0	10.0
m02	70.0	7.2	22.8	75.0	10.0	15.0
m03	63.4	7.0	29.6	70.0	10.0	20.0
m04	68.6	19.0	12.4	68.0	24.5	7.5
m08	80.0	15.0	5.0	78.0	19.0	3.0
m10	92.0	5.0	3.0	91.7	6.5	1.8
m11	84.0	15.0	1.0	80.7	18.7	0.6
m12	82.0	15.0	3.0	79.3	18.9	1.8
m13	62.5	30.0	7.5	58.8	36.7	4.5
m14	60.0	20.0	20.0	61.0	26.5	12.5
m19	62.5	25.0	12.5	60.9	31.6	7.5
m20	70.0	2.0	28.0	78.0	2.9	19.1
m21	98.0	1.5	0.5	97.8	1.9	0.3
Part 2						
m05	50.0	40.0	10.0	46.2	48.1	5.7
m06	40.0	50.0	10.0	36.0	58.5	5.5
m07	20.0	70.0	10.0	17.1	77.7	5.2
m15	40.0	20.0	40.0	44.2	28.7	27.1
m16	27.9	36.6	35.5	28.7	48.9	22.4
m17	40.0	43.0	17.0	37.6	52.6	9.8
m18	35.0	50.0	15.0	32.0	59.6	8.4

experimental techniques described in the next section.

2. Experimental details

2.1. Manufacture and heat treatments

The starting materials employed in the manufacture of the alloys were: zirconium (99.9%–600 ppm wt Fe-200 ppm wt O), tin (99.999 wt%) and iron (99.95 wt%).

The buttons (~8 g) were prepared in an arc furnace with a W electrode and a water-cooled copper crucible, in a high purity argon atmosphere (99.999%). They were re-melted at least four times in order to achieve homogeneity. The buttons were divided in three samples. Two samples were used for the 800 °C or the 900 °C isothermal heat treatments, respectively. The third sample of the button was used for the as-cast characterization.

Prior to heat treatment the samples were carefully cleaned and rinsed, wrapped in tantalum sheets and sealed in silica glass under high purity argon atmosphere. The heat treatments were performed in tubular furnaces with temperature control of ±2 °C. Finally, the samples were water-quenched to room temperature without breaking the containers.

For the two parts of the work a total of 20 ternary alloys were designed and prepared with the mentioned procedures. The chemical compositions (in wt% and at.% of the constituent elements) of these alloys are given in Table 2. They are also indicated as numbered points in the Gibb's triangle of Fig. 1. In the same diagram, the compositions of the binary and ternary phases of interest are shown.

2.2. Sample analyses and characterization

Different experimental techniques were used to identify the composition of the present phases in the samples.

The chemical composition was determined by electron-probe microanalysis, EPMA (Cameca SX-50), at 20 kV with 10 nA of electron beam current. The chamber vacuum was 2×10^{-4} Pa. High purity Zr (99.99 wt%), Sn (99.999 wt%) and Fe (99.999 wt%) were used as standards, and a

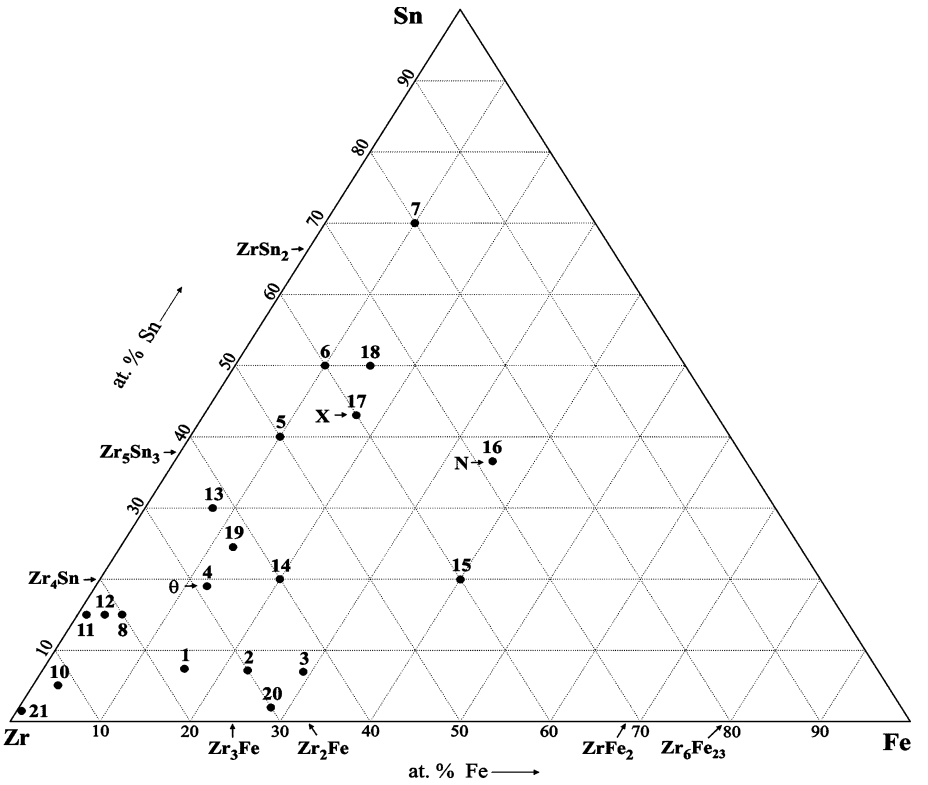

Fig. 1. Zr–Sn–Fe Gibb's triangle. Numbered points represent the composition of the prepared alloys (i.e. point number 1 is the composition of m01 alloy) and the arrows indicate the compositions of the binary and ternary phases of interest.

ZAF correction according to Pouchou and Pichoir was applied to the measured *k*-ratios [9]. The analyzed sample surfaces were prepared by grinding with silicon carbide paper and polished with diamond paste (0.25 μm). No chemical etching was performed over the sample surfaces in order to prevent the re-
precipitation of Sn. The chemical compositions for the present phases were determined by EPMA, by means of a method that allows mapping the fields of one, two and three phases in equilibrium directly over the Gibb's triangle. At least, the results of 200–400 analyses per sample were obtained by scanning three to four lines of about 100–200 μm in length, in steps of 2–4 μm. The method of mapping is fully described by the authors in references [8] and [10]. In Fig. 2, an example of the mapping of EPMA compositions dots generated by this method is shown. The example corresponds to the analyses of m01 alloy heat-treated at 900 °C (its typical microstructure is showed in Fig. 3). As it could be seen in Fig. 2, the EPMA mapping generated a triangular figure, indicating that the sample is inside a three-phases equilibrium field. In the case of samples that are inside triangular three-phase fields, the chemical compositions reported in this work correspond to the average of the EPMA measurements dots considered as vertices of the triangles. When the sample was inside a two-phase field the chemical compositions reported correspond to the average of extreme values of the two-phase field trip. When the sample was in a single-phase region we considered the average of the EPMA measurements only with the intention of assigning an average composition to this phase in the sample,

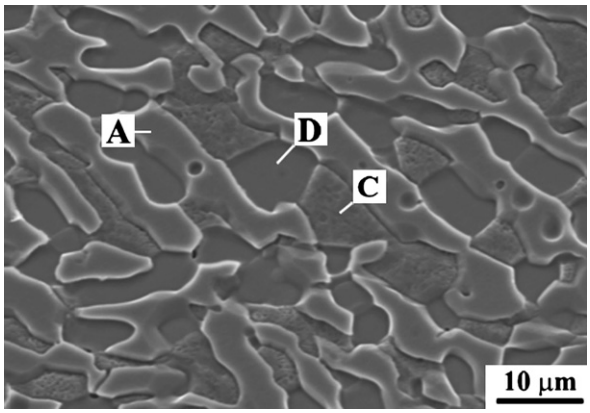

Fig. 3. Scanning electron micrograph of the m01-900 sample, showing a three-phases microstructure: (A) θ-phase, (C) Zr(βt), (D) Zr_2Fe.

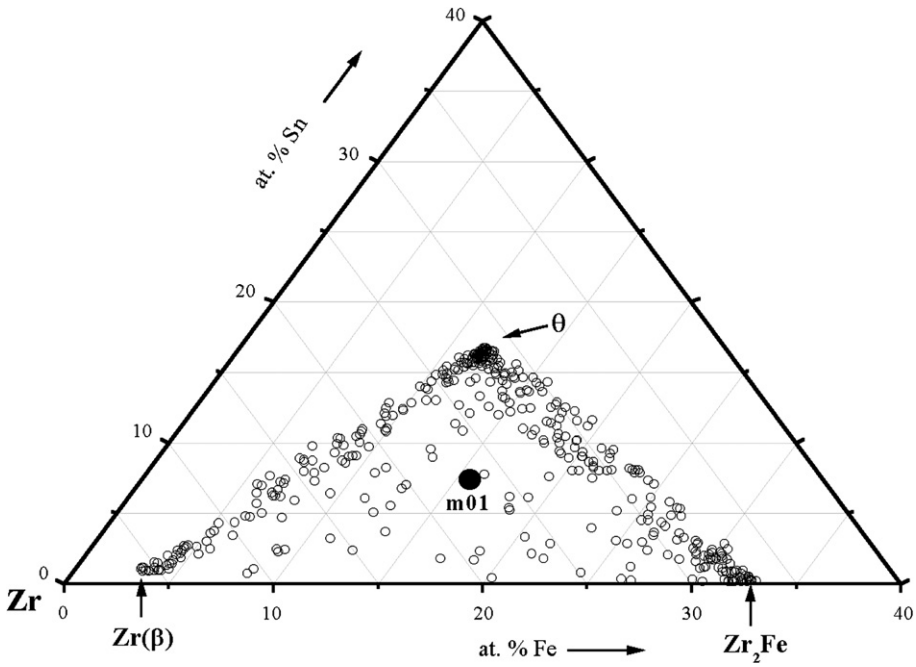

Fig. 2. Mapping of ≈400 EPMA measurements dots, directly drawn on a portion of the Gibb's triangle. They belong to the m01 alloy heat-treated at 900 °C. The triangle vertices correspond to the compositions of the three phases in equilibrium (θ-phase, Zr(β) and Zr_2Fe, in this case).

but the extent of the solubility range, in the case that the phase had it, was determined by means of the observation of the experimental mapping and the analysis of the other samples where the same phase of interest were present but with different compositions.

In addition, metallographic studies and semi-quantitative chemical analyses were performed by a scanning electron microscopy with an X-ray energy dispersive spectrometer (Philips PSEM 500-EDAX). In these cases the analyzed sample surfaces were prepared in the same way as for the EPMA analysis, and a subsequent chemical etching was added to the process (aqueous solution of HNO_3 and HF).

The crystalline structures of the different compounds formed in the samples were identified using X-ray diffraction powder methods at room temperature. Monochromatic Co Kα radiation in a PW 1810 based Philips diffractometer was employed. The measured spectra were compared with theoretical spectra that were calculated with specialized software (PowderCell).

In one of the alloys (m21, the one with the highest content of Zr) an electrical resistance measurement was performed in order to determine phase transformations temperatures. A strip of the alloy of $25 \times 2 \times 0.3$ mm was provided with four spot-welded Zr–1Nb (wt%) wires for the current–voltage measurements. The experimental arrangement for

Table 3
(Part 1) Identified phases, crystalline structure, and zirconium, tin and iron contents measured for 800 °C heat-treated samples

Samples	Heat treatment (°C)/(h)	Identified phases			Composition (at.%)		
		Phase	Crystalline structure				
			Symmetry	Type	Zr	Sn	Fe
		Zr(βt)	Hexagonal	Mg	96.3	2.3	1.4
m01-800	800/680	Zr_3Fe	Orthorhombic	BRe_3	75.3	0.3	24.4
		θ	Hexagonal	Zr_6Al_2Co	71.6	16.6	11.8
		Zr_3Fe	Orthorhombic	BRe_3	75.1	0.3	24.6
m02-800	800/680	Zr_2Fe	Tetragonal	Al_2Cu	66.5	0.4	33.1
		θ	Hexagonal	Zr_6Al_2Co	71.0	17.0	12.0
		Zr_2Fe	Tetragonal	Al_2Cu	66.5	0.4	33.1
m03-800	800/680	$ZrFe_2$	Cubic	$MgCu_2$	34.7	0.3	65.0
		θ	Hexagonal	Zr_6Al_2Co	70.2	17.5	12.3
m04-800	800/680	θ	Hexagonal	Zr_6Al_2Co	70.5	17.9	11.6
		Zr(α)	Hexagonal	Mg	94.4	5.5	0.1
m08-800	800/680	Zr_4Sn	Cubic	Cr_3Si	80.1	19.8	0.1
		θ	Hexagonal	Zr_6Al_2Co	68.2	21.0	10.8
m10-800	800/2107	Zr(βt)	Hexagonal	Mg	96.2	2.5	1.3
		θ	Hexagonal	Zr_6Al_2Co	70.4	18.7	10.9
		Zr(α)	Hexagonal	Mg	92.8	7.0	0.2
m11-800	800/2107	Zr_4Sn	Cubic	Cr_3Si	80.1	19.8	0.1
		θ	Hexagonal	Zr_6Al_2Co	68.5	20.9	10.6
		Zr(α)	Hexagonal	Mg	94.6	5.2	0.2
m12-800	800/2107	Zr_4Sn	Cubic	Cr_3Si	80.0	19.8	0.2
		θ	Hexagonal	Zr_6Al_2Co	68.2	21.2	10.6
		Zr_5Sn_3	Hexagonal	Mn_5Si_3	62.3	37.5	0.2
m13-800	800/2107	$ZrFe_2$	Cubic	$MgCu_2$	35.6	0.4	64.0
		θ	Hexagonal	Zr_6Al_2Co	67.1	21.8	11.1
		Zr_5Sn_3	Hexagonal	Mn_5Si_3	62.2	36.9	0.9
m14-800	800/2000	$ZrFe_2$	Cubic	$MgCu_2$	34.3	0.4	65.3
		θ	Hexagonal	Zr_6Al_2Co	66.7	22.2	11.1
		Zr_5Sn_3	Hexagonal	Mn_5Si_3	62.4	37.5	0.1
m19-800	800/2000	$ZrFe_2$	Cubic	$MgCu_2$	34.4	0.4	65.2
		θ	Hexagonal	Zr_6Al_2Co	66.7	22.3	11.0
		Zr_3Fe	Orthorhombic	BRe_3	75.4	0.3	24.3
m20-800	800/2000	Zr_2Fe	Tetragonal	Al_2Cu	66.5	0.3	33.2
		θ	Hexagonal	Zr_6Al_2Co	71.0	17.0	12.0
m21-800	800/2000	Zr(α)	Hexagonal	Mg	98.5	1.4	0.1
		Zr(βt)	Hexagonal	Mg	97.5	0.9	1.6

The standard deviation is less than 0.3 in all the EPMA measurements.

the high-temperature measurements consisted of a silica glass tube containing the sample connected to a high-vacuum system ($<10^{-4}$ Pa). The temperature of the samples was measured with a Pt/Pt–10 wt% Rh calibrated thermocouple.

3. Results and discussion

3.1. Part 1. 800 °C and 900 °C heat-treated alloys

Table 3 gives the compositions and crystalline structures of the main phases as measured by XRD and EPMA, respectively, on the 800 °C heat-treated samples of part 1. Three intermetallics of the Zr–Fe system (Zr_3Fe, Zr_2Fe and $ZrFe_2$) and two intermetallics of Zr–Sn system (Zr_4Sn and Zr_5Sn_3) were observed in the present experiments of this part. In addition, one ternary compound was observed (θ-phase) and the terminal solid solutions Zr(α) and Zr(β). In fact, the observed Zr(β) phase in the samples was actually the transformed Zr(βt) hexagonal phase, that corresponds to a Widmänstatten-type transformation (diffusion assisted) when cooling from the Zr(β) high temperature phase, and has an average composition very close to the high temperature Zr(β) [11].

From the EPMA results of the samples of this part we found that the single-phase region of the

Table 4
(Part 1) Identified phases, crystalline structure, and zirconium, tin and iron contents measured for 900 °C heat-treated samples

Samples	Heat treatment (°C)/(h)	Identified phases			Composition (at.%)		
		Phase	Crystalline structure				
			Symmetry	Type	Zr	Sn	Fe
		Zr(βt)	Hexagonal	Mg	95.5	1.1	3.4
m01-900	900/432	Zr_2Fe	Tetragonal	Al_2Cu	67.2	0.4	32.4
		θ	Hexagonal	Zr_6Al_2Co	71.5	16.6	11.9
		Zr(βt)	Hexagonal	Mg	95.5	1.1	3.4
m02-900	900/432	Zr_2Fe	Tetragonal	Al_2Cu	67.2	0.4	32.4
		θ	Hexagonal	Zr_6Al_2Co	71.3	16.7	12.0
		Zr_2Fe	Tetragonal	Al_2Cu	66.3	0.4	33.3
m03-900	900/432	$ZrFe_2$	Cubic	$MgCu_2$	33.8	0.4	65.8
		θ	Hexagonal	Zr_6Al_2Co	69.7	18.1	12.2
m04-900	900/432	θ	Hexagonal	Zr_6Al_2Co	67.7	20.4	11.9
		Zr(α)	Hexagonal	Mg	93.8	6.1	0.1
m08-900	900/432	Zr_4Sn	Cubic	Cr_3Si	80.1	19.7	0.2
		θ	Hexagonal	Zr_6Al_2Co	68.6	20.9	10.5
		Zr(α)	Hexagonal	Mg	95.1	4.5	0.4
m10-900	900/1411	Zr(βt)	Hexagonal	Mg	95.7	2.1	2.2
		θ	Hexagonal	Zr_6Al_2Co	69.9	19.2	10.9
		Zr(α)	Hexagonal	Mg	93.8	6.1	0.1
m11-900	900/1411	Zr_4Sn	Cubic	Cr_3Si	80.1	19.7	0.2
		θ	Hexagonal	Zr_6Al_2Co	68.6	20.9	10.5
		Zr(α)	Hexagonal	Mg	93.8	6.1	0.1
m12-900	900/1411	Zr_4Sn	Cubic	Cr_3Si	80.1	19.7	0.2
		θ	Hexagonal	Zr_6Al_2Co	68.6	20.9	10.5
		Zr_5Sn_3	Hexagonal	Mn_5Si_3	61.5	38.2	0.3
m13-900	900/1411	$ZrFe_2$	Cubic	Cu_2Mg	33.3	1.1	65.6
		θ	Hexagonal	Zr_6Al_2Co	66.7	22.0	11.3
		Zr_5Sn_3	Hexagonal	Mn_5Si_3	61.5	38.2	0.3
m14-900	900/1293	$ZrFe_2$	Cubic	Cu_2Mg	33.3	1.1	65.6
		θ	Hexagonal	Zr_6Al_2Co	66.7	22.0	11.3
		Zr_5Sn_3	Hexagonal	Mn_5Si_3	61.5	38.2	0.3
m19-900	900/1293	$ZrFe_2$	Cubic	Cu_2Mg	33.3	1.1	65.6
		θ	Hexagonal	Zr_6Al_2Co	66.7	22.0	11.3
		Zr(βt)	Hexagonal	Mg	95.1	1.5	3.4
m20-900	900/1293	Zr_2Fe	Tetragonal	Al_2Cu	66.7	0.3	33.0
		θ	Hexagonal	Zr_6Al_2Co	71.0	16.4	12.6
m21-900	900/1293	Zr(α)	Hexagonal	Mg	96.8	3.0	0.2
		Zr(βt)	Hexagonal	Mg	98.3	1.0	0.7

The standard deviation is less than 0.3 in all the EPMA measurements.

θ-phase is not a ternary line-compound, as previously reported [1,5], but it extends over a limited solubility range. Table 3 shows that its Zr content varies from 71.6 at.% (measured on the m01-800 sample) to 66.7 at.% (measured on m14-800 and m19-800). On the other hand, the Sn content of this phase varies from 22.3 at.% (m19-800) to 16.6 at.% (m01-800) and the Fe content varies from 12.3 at.% (m03-800) to 10.6 at.% (m11-800 and m12-800).

The Zr_4Sn is an intermetallic compound reported in the Zr–Sn system. This cubic stoichiometric compound is stable up to the peritectoid Zr(β) + $Zr_5Sn_3 \leftrightarrow Zr_4Sn$ decomposition temperature at 1327 °C [11]. On the other hand, the hexagonal line-compound Zr_5Sn_3 is stable up to the congruent melting temperature at 1988 °C [11].

Some authors previously reported and discussed the stability of the Zr_4Sn compound. For instance, in early studies it was not even observed [12], and others studies reported that it was stable only at high temperatures [13–15]. On the other hand, Kwon and Corbett [16] reported that the complete formation of the Zr_4Sn was hard to obtain. A similar conclusion was obtained by Arias and Roberti [17] who reported that the nucleation and growth

Table 5
(Part 2) Identified phases, crystalline structure, and zirconium, tin and iron contents measured for 800 °C heat-treated samples

Samples	Heat treatment (°C)/(h)	Identified phases			Composition (at.%)		
		Phase	Crystalline structure				
			Symmetry	Type	Zr	Sn	Fe
m05-800	800/680	Zr_5Sn_4	Hexagonal	Ti_5Ga_4	53.8	38.1	8.1
		X	n.d.	–	43.6	39.1	17.3
		Zr_5Sn_4	Hexagonal	Ti_5Ga_4	55.4	44.0	0.6
m06-800	800/680	X	n.d.	–	39.4	44.1	16.5
		$ZrSn_2$	Orthorhombic	$TiSi_2$	34.2	65.5	0.3
		$ZrSn_2$	Orthorhombic	$TiSi_2$	33.5	66.1	0.4
m07-800	800/680	Sn	Tetragonal	Sn(β)	0.3	99.5	0.2
		N	n.d.	–	27.3	37.4	35.3
m15-800	800/2000	Zr_5Sn_4	Hexagonal	Ti_5Ga_4	54.1	37.9	8.0
		$ZrFe_2$	Cubic	$MgCu_2$	29.1	10.1	60.8
m16-800	800/2000	N	n.d.	–	27.3	37.0	35.7
m17-800	800/2000	X	n.d.	–	39.1	43.8	17.1
		$ZrSn_2$	Orthorhombic	$TiSi_2$	33.9	65.8	0.3
m18-800	800/2000	X	n.d.	–	38.9	43.6	17.5
		N	n.d.	–	27.9	36.9	35.2

The standard deviation is less than 0.3 in all the EPMA measurements (n.d.: not determined).

Table 6
(Part 2) Identified phases, crystalline structure, and zirconium, tin and iron contents measured for 900 °C heat-treated samples

Samples	Heat treatment (°C)/(h)	Identified phases			Composition (at.%)		
		Phase	Crystalline structure				
			Symmetry	Type	Zr	Sn	Fe
m05-900	900/432	Zr_5Sn_4	Hexagonal	Ti_5Ga_4	54.6	39.0	6.4
		X	n.d.	–	43.6	38.7	17.7
		$ZrSn_2$	Orthorhombic	$TiSi_2$	32.9	67.0	0.1
m07-900	900/432	Sn	Tetragonal	Sn(β)	0.1	99.8	0.1
		N	n.d.	–	27.0	38.0	35.0
m15-900	900/1411	Zr_5Sn_4	Hexagonal	Ti_5Ga_4	54.8	38.8	6.4
		$ZrFe_2$	Cubic	$MgCu_2$	29.9	7.7	62.4
m16-900	900/1411	N	n.d.	–	26.8	37.3	35.9
m17-900	900/1411	X	n.d.	–	40.0	43.1	16.9
		$ZrSn_2$	Orthorhombic	$TiSi_2$	33.9	65.9	0.2
m18-900	900/1411	X	n.d.	–	38.2	43.1	18.7
		N	n.d.	–	28.1	37.1	34.9

The standard deviation is less than 0.3 in all the EPMA measurements (n.d.: not determined).

of this phase is 'sluggish'. Also, it was reported that little amounts of carbon (i.e. 0.37at.%) inhibit the nucleation of this phase [18,19], and Tanner and Levinson emphasized the influence of the Fe in the destabilization of the Zr_4Sn phase in their foundational work on the Zr–Sn–Fe phase diagram [1].

The Zr_5Sn_3 and Zr(α) were observed to be the main phases in the m08, m11 and m12 as-cast alloys. Also, the θ-phase was identified in these three as-cast samples as a minority phase. Only traces of Zr_4Sn were observed in the m12 as-cast alloy.

After the 800 °C heat treatments, the Zr_4Sn phase was observed in the mentioned three samples (Table 3). However, metallographic observations and EPMA measurements, established the presence of very small grains of Zr_5Sn_3 remaining in the microstructure, but in an evident process of dissolution. This process was more visible in m11-800 and m12-800 samples (of longer heat treatments duration than m08-800) where only traces of Zr_5Sn_3 were detected. From these results we conclude that the Zr_4Sn in stable in m08, m11 and m12 at 800 °C.

Table 4 gives the compositions and crystalline structure of the phases as measured by XRD and EPMA, respectively, on the 900 °C heat-treated samples. Two intermetallics of the Zr–Fe system (Zr_2Fe and $ZrFe_2$) and two intermetallics of Zr–Sn system (Zr_4Sn and Zr_5Sn_3) were observed. The ternary θ-phase compound and the solid solutions Zr(α) and Zr(βt) were also observed. With respect to the results obtained at 800 °C, the main difference is that at 900 °C the Zr_3Fe phase was not observed. As shown in Table 4, the m01-900, m02-900 and m20-900 samples have the same three phases in equilibrium. On the other hand, the Zr_5Sn_3 compound observed in the m08, m11 and m12 as-cast samples completely disappeared from these samples after the 900 °C heat treatments.

3.2. Part 2. 800 and 900 °C heat-treated alloys

Tables 5 and 6 give the compositions and crystalline structures of the main phases as measured by XRD and EPMA, respectively, on the heat-treated samples of the part 2.

No important differences were observed between 800 and 900 °C of this part. After the heat treatments the m06 (m06-800), m07 and m18 alloys showed three phases in equilibrium. On the other hand, m05 and m15 alloys showed two phases in equilibrium and m16 and m17 showed only one main phase.

The main source of information on phase relationships for Zr–Sn system is the 1953 work of McPherson and Hansen [20], and they reported fast degradation processes in binary alloy samples in the neighbourhood of Zr_5Sn_3 compound. In the present work, m05 and m06 alloys showed severe experimental difficulties after the heat treatments because they were exceedingly unstable in air. After the characterization (when it was possible) the whole samples disintegrated to powder in few hours. The sample m06-900 could not be analyzed due to the very fast process of degradation (few minutes).

One binary compound of the Zr–Fe system (the $ZrFe_2$ in the m015 heat-treated samples) and two binary compounds of the Zr–Sn system (Zr_5Sn_4 and $ZrSn_2$) were identified in the samples of this part. The Zr_5Sn_4 was identified in the samples m05-800, m05-900, m06-800, m15-800 and m15-900. As an example, Fig. 4 shows the typical microstructure of the m15-900, where the Zr_5Sn_4 phase coexists with $ZrFe_2$ phase. On the other hand, the $ZrSn_2$ was observed in m06-800, m07-800, m07-900, m18-800 and m18-900.

The Zr_5Sn_4 phase was also observed in all the as-cast alloys of this part. There is not complete experimental evidence about the process of formation of this phase. Abriata et al. in their review of the binary Zr–Sn system [11] mention it as a 'probable intermediate phase' of the Ti_5Ga_4 type (first reported by Rossteutscher and Schubert [14]). On the other hand, Kwon and Corbett [16] analyzed the Zr_5Sn_3–Zr_5Sn_4 binary region by means of X-ray diffraction studies and they proposed that these two phases are stoichiometric compounds at

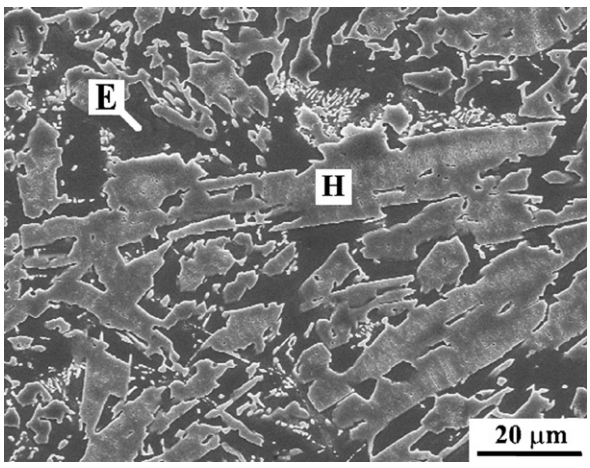

Fig. 4. Scanning electron micrograph of the m15-900 sample, showing a two-phases microstructure: (E) $ZrFe_2$, (F) Zr_5Sn_4.

low temperatures (37.5% Sn content for Zr_5Sn_3 and 44.4% Sn content for Zr_5Sn_4) and that they form a solid solution of the Zr_5Sn_{3+x} type at high temperatures ($T > 1100$ °C). In the present work, the crystalline structure of the Zr_5Sn_4 compound was verified in the m05, m06 and m15 heat-treated samples, where it is present in equilibrium with other phases. Also, in the m16 and m17 heat-treated samples we detected traces corresponding to the Zr_5Sn_4. From the Fe contents observed on the Zr_5Sn_4 phase (measured on m05 and m15 heat-treated samples), we suggest that this phase has a limited range of solubilty. These Fe contents extend up to 8.1 at.% at 800 °C and up to 6.4 at.% at 900 °C (Tables 5 and 6).

On the other hand, the m15-800 and m15-900 samples showed a significant solubility of Sn in the $ZrFe_2$ phase (Tables 5 and 6). We must point out that the solubility of Sn in the $ZrFe_2$ corresponding to the part 1 heat-treated samples m03, m13 m14 and m19 was small (Tables 3 and 4).

The $ZrSn_2$ phase, previously mentioned, is a face centered orthorhombic compound, stable up to the peritectic $Zr_5Sn_3 + L \leftrightarrow ZrSn_2$ decomposition reaction at 1142 °C, with a 66.7 at.% content of Sn, according to [11]. This compound was observed in all the as-cast alloys of this part 2 except in m05 and m15. After the treatments it only appears in three-phase equilibrium fields of the m06, m07 and m18 samples. In the m16 and m17 heat-treated samples it was only detected as traces.

In this region, the authors previously observed two ternary compounds: N-phase and X-phase [7,8]. In the present work we report the composition, some X-ray diffraction results, the metallography of this phases and the relationship between them with the high Sn binary Zr–Sn compounds. As an example, Fig. 5 shows the X and the N-phase typical metallographic aspect, accompanied in this case by the $ZrSn_2$ phase in the m18-900 sample. In the as-cast samples corresponding to this part of the work, the N-phase was observed in all the cases; on the other hand the X-phase was detected in all the cases except in the m07 as-cast sample. After the heat treatments at 800 and 900 °C, the N-phase disappears in m05, m06 (800 °C), and m15, and the X-phase disappears in m15. The X-ray diffraction analyses in different samples of this work indicate that some of the peaks that would correspond to the N-phase are located in 2Θ equal to 42.3°, 43.3°, 44.8°, 45.8°, 46.4°, 47.8° and 48.7°. On the other hand the main peaks that would correspond to the X-phase are in 2Θ equal to 36.6°, 38.6°, 39.8°, 40.8°, 42.4°, 43.8°, 44.3°, 45.3° and 47.3°.

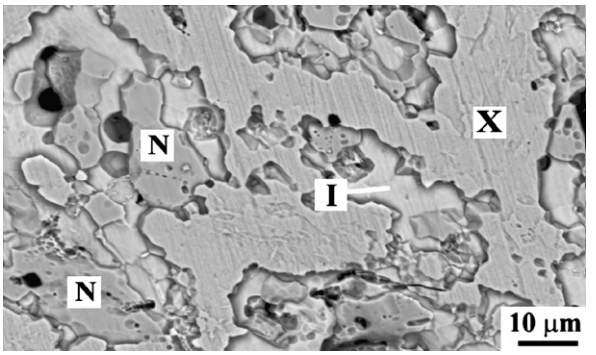

Fig. 5. Scanning electron micrograph of the m18-900 sample, showing a three-phases microstructure: (I) $ZrSn_2$, (N) N-phase, (X) X-phase.

3.3. Zr-rich corner. Resistance measurements

The Zr-rich corner is of most technological importance, so we decided to make a review of this region analyzing the m21 alloy and using the results of the heat-treated m01, m02, m20, m08, m10, m11 and m12 samples.

Tanner and Levinson [1] studied the Zr-rich corner of this ternary phase diagram for the first time. They made and analyzed an important number of ternary alloys but, as it was mentioned above in the Introduction, they did not recognize the presence of the binary compounds Zr_3Fe, Zr_2Fe and reported an instability of Zr_4Sn. On the other hand, in the review of Raghavan [6] no details of this corner are shown in the 'tentative' 700 and 1100 °C isothermal sections. The alloy m21 was made in order to add experimental data for the diagram adjustment of this region. The EPMA results of the m21 heat-treated samples (m21-800 and m21-900) are shown in Tables 3 and 4. In addition, a measurement of the variation of the electrical resistance against the temperature was performed on the m21 alloy with the intention to identify the phase boundaries Zr(α)/Zr(β) in this region [17,21]. According to our experiments, the $Zr(\alpha) \leftrightarrow Zr(\alpha) + Zr(\beta)$ transformation temperature occurs at 790 ± 5 °C, and the $Zr(\alpha) + Zr(\beta) \leftrightarrow Zr(\beta)$ one occurs at 916 ± 5 °C. These results (added to the EPMA and metallographic ones) confirmed that the analyzed alloy is, at 800 °C and at 900 °C, located into the two-phase field $[Zr(\alpha) + Zr(\beta)]$. The relative amounts of each phase were estimated, as a first

approach, using the Zr(α)/Zr(β) ratio at different temperatures from the R vs. T curves [21]. Thus, at 800 °C the Z(α)/Zr(β) ratio is ~0.9, whereas at 900 °C the same ratio is ~0.3.

3.4. Partial experimental phase diagrams

Figs. 6(a) and 7(a) show the Zr–Sn–Fe partial experimental phase diagrams as determined in the

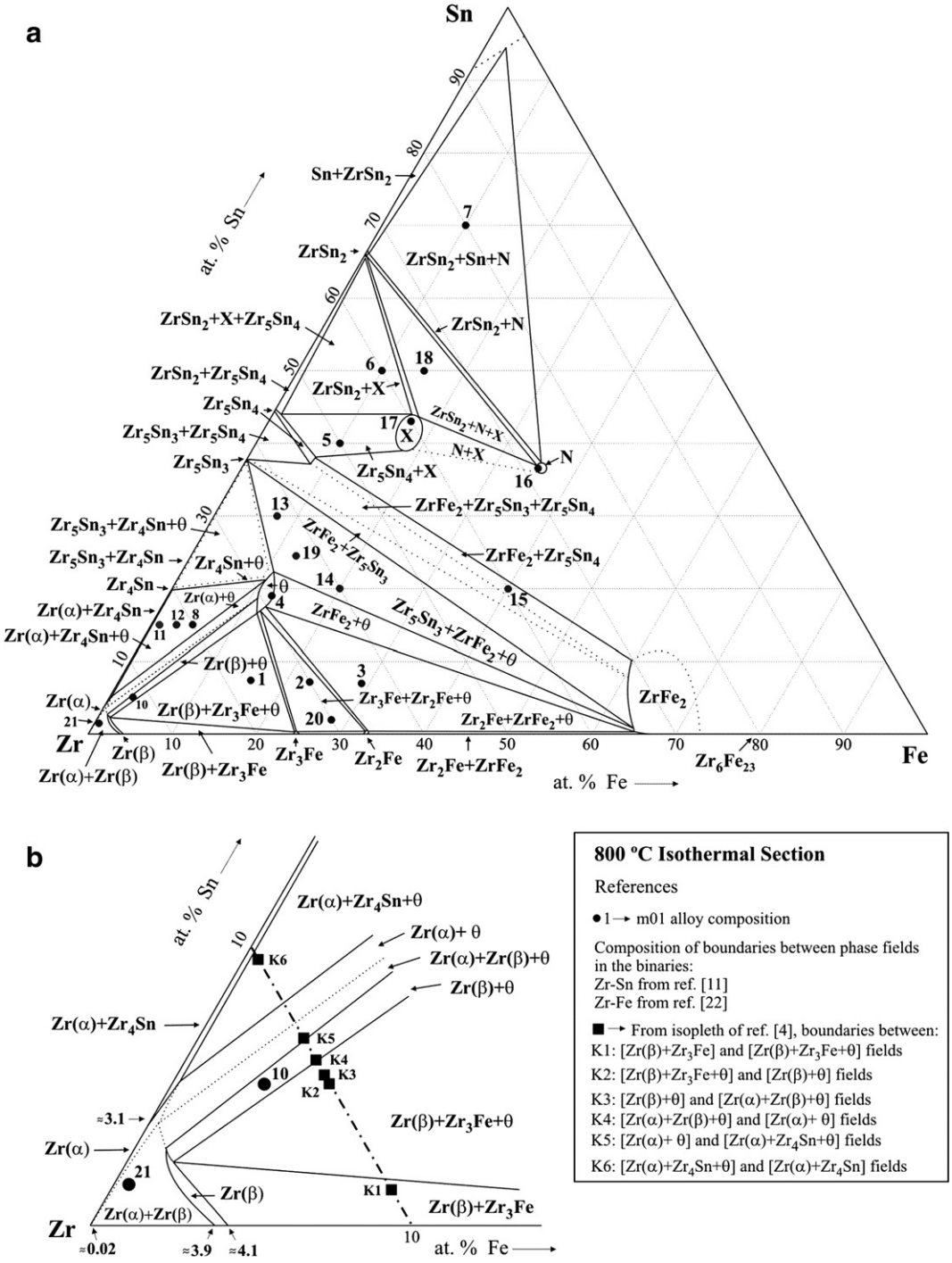

Fig. 6. (a) Isothermal section at 800 °C. (b) Details of Zr-rich region. Phase boundaries: (—) measured, (---) probable. Numbered points represent the composition of the prepared alloys (i.e. point number 1 is the composition of m01 alloy).

present study. They correspond to 800 and 900 °C isothermal sections respectively. The limits of existence of phases, the composition of the phases considered in equilibrium (triangle vertices or limits of two-phase fields) and the composition of the analyzed alloys (numbered points) are indicated in the diagrams.

Figs. 6(b) and 7(b) show more details of the Zr-rich corner. In order to delineate this region, in addition to our experimental results, extra

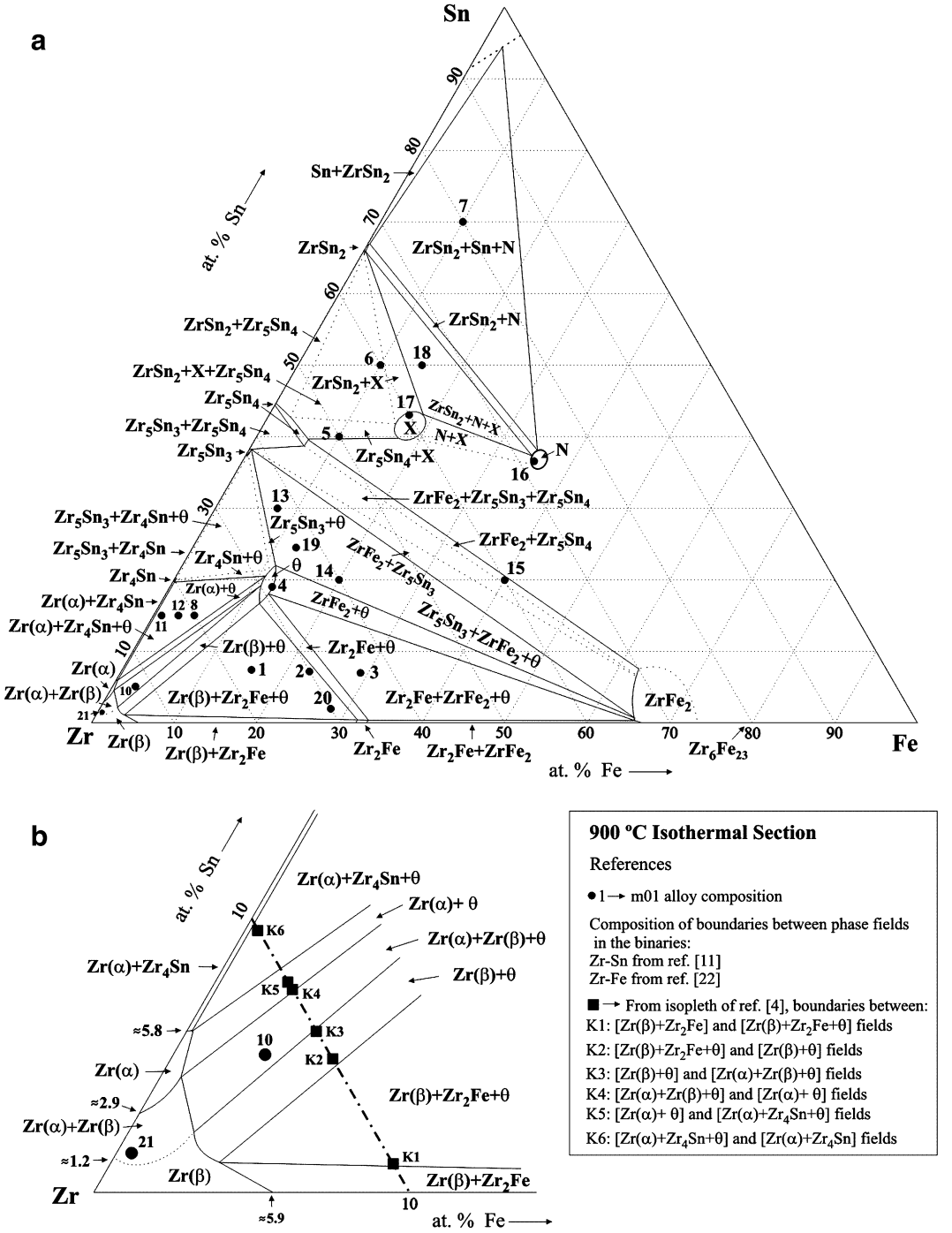

Fig. 7. (a) Isothermal section at 900 °C. (b) Details of Zr-rich region. Phase boundaries: (—) measured, (---) probable. Numbered points represent the composition of the prepared alloys.

information of the binary diagrams Zr–Sn [11] and Zr–Fe [22] was considered. The general aspect of the diagram in this region is similar to those proposed by Tanner and Levinson [1], although with slight differences in the Zr(α), Zr(β), and Zr(α) + Zr(β) field boundaries. In the same figures, the intersections between the isopleth proposed by Korotkova [4] and the present isothermal sections are shown. Some differences in the traces of the phase fields' boundaries are observed, more remarkable in the 800 °C case.

4. Conclusions

We present the experimental partial Zr–Sn–Fe phase diagrams at 800 and 900 °C. From the study of the analyzed region we extract the following conclusions:

(a) The knowledge of the θ- and N-phase was deepened. The former presents an extended single-phase region.
(b) The X-phase, not reported in the literature, was characterized. It presents an extended single-phase region.
(c) The Zr_4Sn and Zr_5Sn_3 phases show low solubility of Fe, and the Zr_3Fe, Zr_2Fe and Zr_3Fe phases show low solubility of Sn in the samples of part 1.
(d) An important solubility of Fe in the Zr_5Sn_4 phase and of Sn in the $ZrFe_2$ was measured in the samples of part 2.
(e) A very 'sluggish' behavior in the nucleation and growth processes of the Zr_4Sn compound was verified.

Acknowledgements

This work was partially supported by the Consejo de Investigaciones of the Universidad Nacional de Tucumán (CIUNT), the Consejo Nacional de Investigaciones Científicas y Tecnológicas (CONICET) and the Agencia Nacional de Promoción Científica y Tecnológica, República Argentina.

References

[1] L.E. Tanner, D.W. Levinson, Trans. ASM 52 (1960) 1115.
[2] E.T. Hayes, A.H. Roberson, W.L. O'Brien, Trans. ASM 43 (1951) 888.
[3] D.L. Kudryatsev, I.A. Tregubov, in: Physical Chemistry of Zr alloys, USSR Sciences Academy, Moscow, 1968, p. 133 (in Russian).
[4] N.V. Korotkova, Russ. Metall. 5 (1990) 201.
[5] Y. Kwon, S. Sevov, J.D. Corbett, Chem. Mater. 2 (1990) 550.
[6] V. Raghavan (Ed.), Phase Diagrams of Ternary Iron Alloys, Part 6, Indian Institute of Metals, Calcutta, 1992, p. 1199.
[7] N. Nieva, D. Arias, J. Nucl. Mater. 277 (2000) 120.
[8] N. Nieva, D. Arias, in: CALPHAD XXX, York, England, 2001.
[9] J.L. Pouchou, F. Pichoir, La Recherche Aerospatiale 3 (1984) 13.
[10] N. Nieva, M. Canay, D. Arias, An. J. SAM-CONAMET/Simp. Mater. 1 (2003) 373.
[11] J.P. Abriata, J.C. Bolcich, D. Arias, Bull. Alloy Phase Diagrams 4 (1983) 147.
[12] H. Nowotny, H. Schachner, Monatsh. Chem. 84 (1953) 169.
[13] K. Schubert, T.R. Anantharaman, H.O.K. Ata, H.G. Meissner, M. Potzschke, W. Rossteustcher, E. Stolz, Naturwissenschaften 47 (1960) 512.
[14] W. Rossteutscher, K. Schubert, Z. Metallkd. 56 (1965) 813.
[15] H.L. Luo, E. Vielhaber, E.Z. Corenzwit, Z. Phys. 230 (1970) 443.
[16] Y. Kwon, J.D. Corbett, Chem. Mater. 2 (1990) 27.
[17] D. Arias, L. Roberti, J. Nucl. Mater. 118 (1983) 143.
[18] O.N. Carlson, H.A. Wilhelm, USAEC Report No. TID.5061.
[19] O.N. Carlson, J.F. Smith, Bull. Alloy Phase Diagrams 8 (1987) 208.
[20] D.J. McPherson, M. Hansen, Trans. Am. Soc. Met. 45 (1953) 915.
[21] M. Canay, C.A. Danón, D. Arias, J. Nucl. Mater. 280 (2000) 365.
[22] D. Arias, M.S. Granovsky, J.P. Abriata, in: H. Okamoto (Ed.), Phase Diagrams of Binary Iron Alloys, ASM Int., Materials Park, 1993, p. 467.